

Title	Solution and surfactant-free growth of supported high index facet SERS active nanoparticles of rhenium by phase demixing
Authors	Valenzuela, Carlos Díaz;Valenzuela, María Luisa;Caceres, S.;O'Dwyer, Colm
Publication date	2012-11-21
Original Citation	Valenzuela, C. D., Valenzuela, M. L., Caceres, S. and O'Dwyer, C. (2013) 'Solution and surfactant-free growth of supported high index facet SERS active nanoparticles of rhenium by phase demixing', Journal of Materials Chemistry A, 1(5), pp. 1566-1572.
Type of publication	Article (peer-reviewed)
Link to publisher's version	10.1039/C2TA00262K
Rights	© The Royal Society of Chemistry 2013
Download date	2024-04-25 07:05:01
Item downloaded from	https://hdl.handle.net/10468/6164

Cite this: DOI: 10.1039/c0xx00000x

www.rsc.org/xxxxxx

ARTICLE TYPE

Solution and surfactant-free growth of supported high index facet SERS active nanoparticles of Rhenium by phase demixing

C. Díaz Valenzuela,^{*a} M. L. Valenzuela,^b S. Caceres,^a and C. O'Dwyer^{*c,d}

Received (in XXX, XXX) Xth XXXXXXXXXX 20XX, Accepted Xth XXXXXXXXXX 20XX

DOI: 10.1039/b000000x

Stable, high-index facet Re nanoparticles have been grown by a solid state synthetic method, negating the need for solutions or surfactants to control seeding, supracrystallization and NP shape. By using mixtures of $\text{K}[\text{ReO}_4]$ and the cyclic triphosphazene $[\text{NP}(\text{O}_2\text{C}_{12}\text{H}_8)]_3$, high-index facet nanoparticles and nanocrystals ~ 3 nm in size can be seeded and grown from drop-cast films and powders due to phase demixing of a metastable metallopolymer. NP dispersions are formed directly within a graphitic carbon support that liquefies, allowing NP coarsening and ripening, and the eventual formation of a solidified graphitic support filled with crystals. Successful growth of mesoscale supracrystals of Re also occurs from ripening of nucleated NP seeds, incubated within a spinodally decomposed solid support that patterns the surface. The supported Re NP dispersions also exhibit surface enhanced Raman scattering within a graphitic matrix.

1. Introduction

Metallic nanostructures with a variety of uniquely functional shapes^{1, 2} are known to show useful optical, catalytic³ and (electro)chemical benefits and can enhance the development of new chemicals, energy storage paradigms, important chemical and catalytic functions^{3, 4} and biomedical science^{1, 5, 6}. Their growth, however, is mostly limited to solution based bottom-up approaches, especially where size and shape control are important⁷. There has been immense progress recently in metallic crystal growth^{8, 9}, where size dispersion and complex shape control¹⁰ has poignancy for advanced catalytic and related applications. Novel microscopy methods have been developed to monitor nanocrystal growth^{11, 12}, and the recent developments and the development and control of high index facet NPs and crystals from many metals, which have a higher free surface energy, have potentially significant industrial potential as well as being a test-bed for new, artificially tailored nano- and mesoscopic supracrystals.

For the vast majority of nanocrystal and nanoparticle syntheses, and even for high index particle growth¹³ and the new series of metallic supracrystals recently reported¹⁴, their realization is done in liquids and optimized with precisely defined single crystal seed structures and shapes. Growth from controlled seeding and supracrystallization in the solid state could give nanoscale as 3D matrices and drop-cast layers with translational electrical, optical, and chemical properties¹⁵⁻¹⁸. High index and non-spherical NPs can often showed significant surface enhanced Raman scattering (SERS) activity¹⁹, through chemical and electromagnetic means, and high index faceting potentially allows for proximal particle dispersions of metals that normally do not support surface plasmon polaritons, to show SERS.

Recently, graphene has shown promise for high speed photodetectors²⁰ by plasmonic interactions from nanoscale metals, and next-generation photocatalysts,²¹ and more recent work has identified new roughened surfaces and similar structures for SERS of coinage and noble metals^{22, 23}. Previous work on any form a layered carbon or graphene-metallic NP composites have focused on SERS from Au NPs²⁴. The primary challenge is the incorporation and size and proximity dispersion of the metallic NPs within the graphitic host; graphene and reduced graphene oxide substrates or layered carbons offer efficient absorption towards many molecules²⁵, which the method here achieves in a single step.

Supported Rhenium itself has useful catalytic properties for ammonia synthesis²⁶, glycerol conversion, and other hydrocarbon transformations such as *e.g.* hydrodesulfurization and hydrodenitrogenation²⁷. Rhenium is also a high-temperature superalloy component²⁸ employed in rotating elements of aircraft engines, and for enhancement of interfacial properties of microelectronic conductors. Rhenium has largely been ignored for seed-mediated synthesis and recent reports confirm rather large nanoparticle²⁹ formation in solution using ligands, such as those prepared from $\text{ReCl}(\text{CO})_3(\text{N},\text{N})_{10}$ and $\text{Re}_2(\text{CO})_{10}$ ³⁰ using ionic liquids as stabilizing agents.

Here, we report a solution-free, solid state approach to supported high-index facet Re NPs and supracrystals, stably formed during thermolytic demixing and dewetting of a metastable $\text{K}[\text{ReO}_4]/[\text{NP}(\text{O}_2\text{C}_{12}\text{H}_8)]_3$ mixture, or directly as powders. High-index facet NPs and nanocrystals ~ 3 nm in size can be formed from both films and powders due to phase demixing of a metallopolymer, and supracrystals are shown to ripen from nucleated NP seeds, incubated within a spinodally decomposed, solidified carbon support. A Methyl Violet 10B

functionalised NP-infiltrated porous graphitic support is also demonstrated to give significant surface enhanced Raman scattering.

2. Experimental section

2.1 Synthetic procedure

All syntheses were carried out in a dry, oxygen-free, nitrogen atmosphere using standard Schlenk techniques. $\text{K}[\text{ReO}_4]$ was donated by Prof. H. Klahn from PUCV, Chile. $[\text{NP}(\text{O}_2\text{C}_{12}\text{H}_8)]_3$ was prepared using literature procedures³¹.

2.2 Preparation of the mixtures

The mixtures of $\text{K}[\text{ReO}_4]$ (0.1g., 0.354 mmol) and the cyclotriphosphazene $[\text{NP}(\text{O}_2\text{C}_{12}\text{H}_8)]_3$ (1.19g., 1.73 mmol) for the 1:5 molar ratio and of $\text{K}[\text{ReO}_4]$ (0.03g., 0.103 mmol) and $[\text{NP}(\text{O}_2\text{C}_{12}\text{H}_8)]_3$ (0.7g., 1.018 mmol) for the 1:10 molar ratio, were dissolved in dichloromethane, stirred for 24 hours and evaporated in a vacuum until dry. The pyrolysis experiments were made by pouring a weighed portion (0.05–0.15 g) of the respective mixtures of $\text{K}[\text{ReO}_4]/[\text{NP}(\text{O}_2\text{C}_{12}\text{H}_8)]_3$ in molar ratio 1:10 or 1:5 into aluminum oxide boats that were placed in a box furnace (Daihan oven model FHP-12) and heated from 25 to 300 °C and then to 800 °C, with subsequent for 2 h. The heating rate was maintained at 10 °C/min. Additionally for the HRSEM and HRTEM measurements, a drop of the $\text{K}[\text{ReO}_4]/[\text{NP}(\text{O}_2\text{C}_{12}\text{H}_8)]_3$ mixtures in CH_2Cl_2 was placed on the Si or SiO_2 wafer (400 nm thermally grown SiO_2 and the solvent evaporated following a published procedure. After this the wafer coupons containing drop-cast precursors, were pyrolyzed at 800 °C in air.

2.3 Methods of characterization

X-ray diffraction (XRD) was carried out at room temperature on a Siemens D-5000 diffractometer in θ - 2θ geometry. The XRD data was collected using $\text{Cu K}\alpha$ radiation (40 kV and 30 mA). Scanning electron microscopy (SEM) and energy dispersive X-ray analysis (EDX) were acquired with a Hitachi SU-70 FESEM operating at 10 kV equipped with an Oxford Instruments X-max 50 mm² solid-state EDX detector. Transmission electron microscopy (TEM) was carried out on a JEOL JEM-2011 using a LaB_6 filament operating at 200 kV. STEM imaging was performed using a JEOL JEM-2100F in dark field conditions. The finely powdered samples were dispersed in n-hexane and isopropanol, dropped on a conventional holey carbon copper grid and dried under a lamp. TEM image measurements were made using DigitalMicrograph™ software with a Gatan Multiscan 794 CCD Camera.

Raman scattering was conducted with a Horiba Jobin Yvon T64000 spectrometer using 532 nm incident light. Optical imaging was performed using a Zeiss AxioImager A1.m optical microscope in bright field and differential interference contrast modes. SERS measurements were carried out using a Horiba Jobin-Yvon T64000 Triple Raman spectrometer attached to an Olympus confocal optical microscope. Excitation was provided by a 633 nm He-Ne laser. The spectra were typically acquired with a 5 s exposure time and a laser power of 5 mW (at 633 nm) to avoid organic dye burning. A 50 × objective with a numerical aperture of 0.75 was used for all Raman scattering measurements. Methyl Violet 10B was used as the probe molecule. The MV 10B

reagents were dissolved into pure deionized water (18.3 MΩ) and ethanol. The patterned sample was immersed for 1h in the dye solution for sufficient molecule adsorption before SERS measurements, and subsequently rinsed with deionized water.

Measurement of known concentrations of dye within Re-free carbon supports were used as control samples to confirm that scattering enhancement came from SERS of Re-containing regions of the porous carbon.

3. Results and discussion

3.1 Supracrystal and nanoparticle growth

Using a 1:5 mixture ratio, the highest loading of Re NPs is found as a powder and a NP-carbon deposit on substrates. X-ray diffraction (Fig. 1) identified hexagonal single-crystal Re from both methods. In Fig. 1a, SEM shows that the single crystals formed on Si are ~500 nm in size with an unusual, yet characteristic onion- or nautilus-like layering. When formed on surfaces, the crystals observed in Figs 1a and b are always found at the mixture-air interface. Smaller NPs are typically found at the air interface, but also embedded within the carbon support (Fig. 1c).

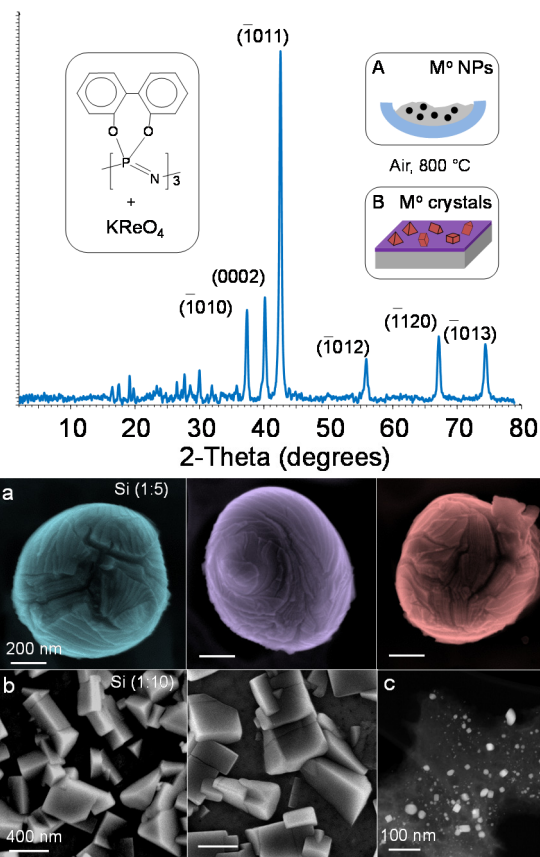


Fig. 1 Scheme of the cyclotriphosphazene/Re salt mixture used and (A) crucible and (B) substrate methods for pyrolysis following suitable drop casting methods. The X-ray diffraction pattern of the bulk pyrolytic product confirms single crystal Re formation with space group $P63/mmc$ and cell parameters $a = 0.276$ nm and $c = 0.445$ nm, (JCPDS #00-001-1231). (a) Layered spherical single crystals of Re formed from demixed drop-cast films at 1:5 ratio and (b) Re crystals formed on Si and SiO_2 from 1:10 ratios (c) HRSTEM image of interspersed Re NPs in the carbon support.

The circular particles formed by thermolysis of a drop-cast layer (Fig. 1a), have an open, layered structure with edge sites, steps and surface porosity. When the relative amount of Re is halved, we observe from the same mechanism by ripening a larger volumetric density of NPs diffusing toward the nucleation site. As seen in Fig. 1b, larger faceted polyhedral supracrystals form from the demixing biphasic composite. As detailed further on, the merging of two heterogeneous process into a single homogeneous crystals growth allow for crystallization of the NPs and large crystals evolve from a pin-holed carbon underlayer, always at the air interface. Dark-field HRSTEM analysis of the carbon matrix confirms crystal growth within the support, from the decomposed cyclotriphosphazene (Fig. 1c).

3.2 Carbon-supported high-index NP formation

The resulting bicontinuous metallopolymer also allows very small Re NPs to form. Figure 2 shows NPs with a range of sizes from pyrolysis of a 1:5 $\text{K}[\text{ReO}_4]/[\text{NP}(\text{O}_2\text{C}_{12}\text{H}_8)_3]$ precursor mixture. Analysis of >950 particles from surrounding regions of the carbon support confirms that the mean diameter of the NPs is 2.9 nm (when the few particles >15 nm are ignored). HRTEM EDX (Fig. 2b and SI Fig. S1) also confirms pure Re formation after reduction from perhenates. For the Re NPs reported here, 86% of the NPs are found in the range 2 – 5 nm, 12% between 5 – 12 nm and 2% of NPs with characteristic dimensions >20 nm. Detailed examination shows that all NPs formed on the lengths scale of 0.5 – 5 nm maintain stable, high-index faceting, and we find no evidence of stacking faults, micro-twinning or other crystal defects in the NPs.

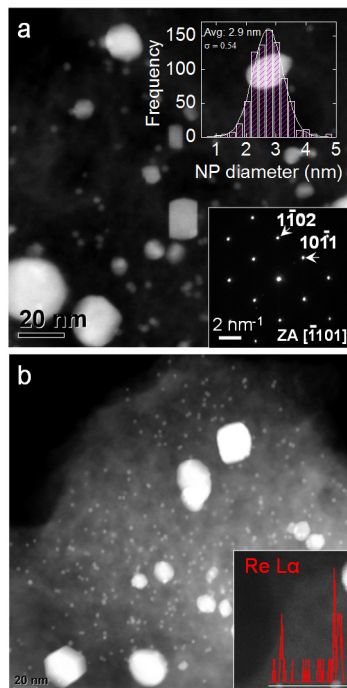


Fig. 2 (a) STEM image of Re crystals, electron diffraction pattern along the $[-1101]$ zone axis confirming hexagonal Re. (Inset) Overall NP size distribution of interspersed Re NPs from several regions in the carbon support. (b) STEM image of RE NP uniformly dispersed within the graphitic carbon support. The large crystals from the polymer-air interface are seen in this carbonaceous slice from the top surface. (Inset) TEM EDX confirming Re content in ~ 2 nm Re NPs.

The lattice resolution HRTEM image in Fig. 3a and corresponding electron diffraction pattern identify the Re hexagonal unit cell with space group $P63/mmc$. We typically find that the Re NPs are terminated with high index planes and often contain piecewise smooth curved edges. The Re NPs are also stable and retain their high index facet shape within the host. Figure 3b shows the edges of nanocrystals with faceting resulting from surfaces constructed from microfacets forming a $(0002) \rightarrow (03-3-7) \rightarrow (01-17)$ edge termination set. The $(03-3-7)$ facet, for example, is comprised of a periodic $(01-1-2) + (01-1-2) + (01-1-3)$ micro-facet set. With a high density of low coordination atoms, the $(03-3-7)$ facet can contain $\sim 5 \times 10^{14}$ step atoms cm^{-2} .

High index faceting can result through solid state diffusion-mediated coarsening mechanisms of Re atomic clusters, giving non-thermodynamically favourable shapes with high angles found between crystal planes (Fig. 3c). This occurs because unlike NPs that coarsen from within thin liquid polymer film systems or in solutions,^{34, 35} the growing NPs from diffusing Re atoms are eventually pinned within a porous solid state carbon support.

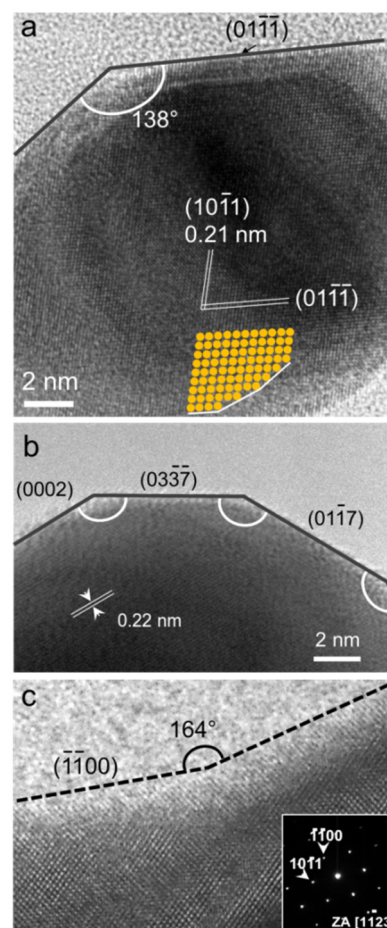


Fig. 3 HRTEM images of (a) a single Re NP and (b,c) the edges of high-index NP facets of similar single crystal Re NPs. (Inset) electron diffraction pattern of hexagonal Re, space group $P63/mmc$ and cell parameters $a = 0.276$ nm and $c = 0.445$ nm.

All crystals formed by this approach coalesce and grow from pinhole voids in the carbonizing organic matter, mostly during its time as a liquid prior to carbonization and solidification. Figure

4a shows one layered circular crystal formed the pinhole in the supporting carbon. The pinholes are formed when the polymer is briefly liquefied (but stabilized by the presence of Re NPs) during heating and are similar to spinodal dewetting in composite polymer films containing nano-inclusions^{12, 34}.

3.3 NP coarsening, crystal seed incubation and ripening

During pyrolysis, the polymer component of mixture undergoes decarbonylation and decomposition (see Supporting Information section S1). A stable solid matrix forms³⁶ which is not lost as a volatile in the first stage of annealing. During this carbonization process, some carbon monoxide³⁷ is also produced which eventually reduces the perrhenate ions to Re, which has a relatively low standard reduction potential of 0.300 V²⁹. As the material solidifies, the instability cause by decomposition processes in the host never fully develops and the layer is essentially a 'frozen-in' porous matrix³⁸⁻⁴⁰ in which Re association occurs to ripen into high index NPs, without needing electrochemical surface reconstruction⁴¹, growth rate-altering surfactants, or co-reduction of species^{42, 43}.

The holes in the solid support act as a nucleation point for the coalescence³⁵ (see Supporting Information, Fig. S1) and NPs grow as the demixing process evolves. This specific cyclic matrix formation of layered carbon can be seen in the STEM image in Fig. 5b2, Fig. 1c and in Supporting Information, Fig. S1. Characteristically for nucleation-driven demixing process, we also observe NPs around the rim of the holes (which is within the polymer; the clustering of NPs is also found around the rims of the surface pinholes in Fig. 4a). It is at this stage, the mixture contains NPs of Re. The carbon surrounding the crystal was also investigated by STEM and is devoid of NPs in the material between pinholes after complete reaction.

For lower Re quantities, such as the 1:10 $\text{K}[\text{ReO}_4]/[\text{NP}(\text{O}_2\text{C}_{12}\text{H}_8)]_3$ mixture drop-cast as a thin film, the resulting crystals are nucleated around and within holes (and Fig. 5b2 and Supporting Information), but at the surface-air interface, and subsequent growth allows the definition of polyhedral crystals of Re (Fig. 4b). Figure 4c shows the latter stages where the pinholes are formed by spinodal-type instability in the polymer; the avoidance of a nucleation dewetting is likely due to the presence of the Re, as is known from simpler systems such as Au in thin PS films. Crystals form from ripening in these surface holes and complete surface coverage in this manner is possible without polymer dewetting and beading that occurs for liquid polymer films; the carbonization and eventual solidification occurs, but can also occur for beaded polymer regions – the NPs presence and coarsening prevents this. As is characteristic of spinodal decomposition, the diameter of pinholes in the carbon is identical and the uniformity of Re dispersion allows self-similar crystal to form within the solidified polymer instability. The back-scattered SEM image in Fig. 4c (inset) shows the characteristic nucleation of Re NP around the pinhole rim prior to seeding and subsequent growth.

NPs are found with a higher density throughout the support (Fig. 1) when the length of pyrolysis time prevents full ripening of all NPs into larger crystals. No polycrystalline particles are formed, and all metal ions form supracrystals rather than aggregates; the Re never melts as its bulk melting temperature of 3185 °C (second highest of all metals) remains above the

pyrolysis temperature even accounting for smaller size-dependent melting point depression in a thermally conductive carbon host⁴⁴.

Many related but simpler liquid polymer systems have been investigated⁴⁵⁻⁴⁸ and the kinetics of NP coarsening in polymers and in organic molecule-passivated NP assemblies at least, is well established. The process occurring here and the eventual solidification of the carbon matrix requires modified theoretical approaches to describe (and help develop) the variation in topological NP ordering and ripening, particularly for the development of functionally important high-index facets in the absence of definitive synthetic passivation protocols.

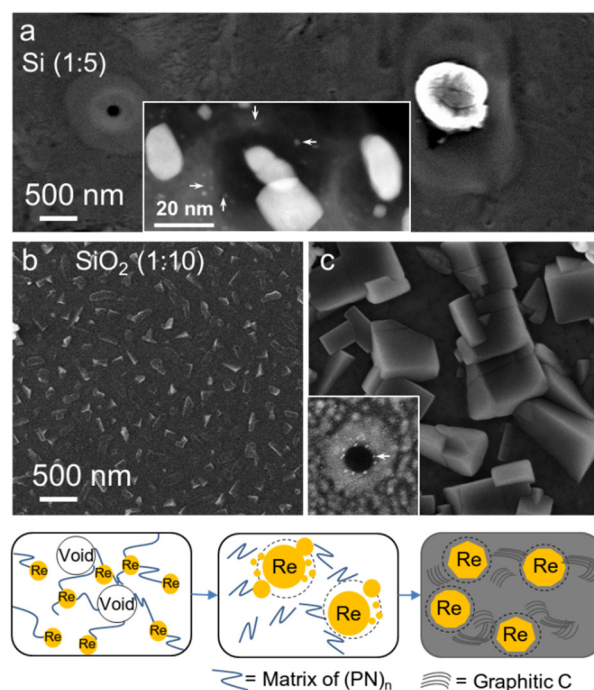


Fig. 4 (a) SEM image of pinholes within carbonized polymer with Re crystal nucleated and incubated within. (Inset) HRSTEM image of cyclomatrix holes within the support. (b) Initial and (c) final stage of Re crystal growth from the drop-cast film. All arrows point to Re NPs. The schematic underneath depicts the salient features of NP coarsening and ripening in parallel with decomposition of the polymer after demixing, to a layered graphitic support.

We also conducted Raman scattering investigations of the carbon support structure that forms. Figure 5 shows spectra for: (a) the surface-air interface (Figs a1-3) and (b) within the support (Figs b1-3). The surface of the carbon matrix (Fig. 5a1 and a2) shows a convoluted D- and G-band pair; convoluted scattered phonon processes describe a mixture of 2D and 3D graphite where the D-band is attributed to curved and disordered graphite sheets and the G-band is characteristic of layered graphite⁴⁹. Future solid state precursor design could allow NP dispersion control by altering the decomposition to get cross-linking polymeric chains (from polymeric precursors to give inorganic foams) or cyclomatrix formation (from cyclic oligomeric precursors to give 2D networks of nanoparticles).

Micro-Raman analysis of localized regions of NP-free cyclomatrix-like carbon (Fig. 5b1-3), shows that a higher quality and density of layered graphite is formed. The 2D band correlates to stacking order and number of layered graphitic sheets; in Fig.

5b₃, the single-peak 2D band indicates a low number of graphitic layers. The D+G band at ~2950 cm⁻¹ (Figs 5a₃ and b₃) indicates the support contains very disordered, randomly oriented, but graphene-like sheets. A corresponding in-plane crystallite size L_a $\sim 4.4(I_G/I_D)$ is estimated to be ~3.7 nm.

The decomposition process clearly results in graphitic carbon in a layered and curved, tortuous form, consistent with decomposition of a cyclotriphosphazene (see Supporting Information section S1). This is found for the carbon support (Fig. 5b₃), and confirms the overall mechanism of decomposition and the formation of holes within the matrix where crystal growth can occur. Nanoparticle dispersion control is likely possible with future development by altering the decomposition to get cross-linking polymeric chains (from polymeric precursors to give inorganic foams) or cyclomatrix formation (from cyclic oligomeric precursors to give 2D networks of NPs).

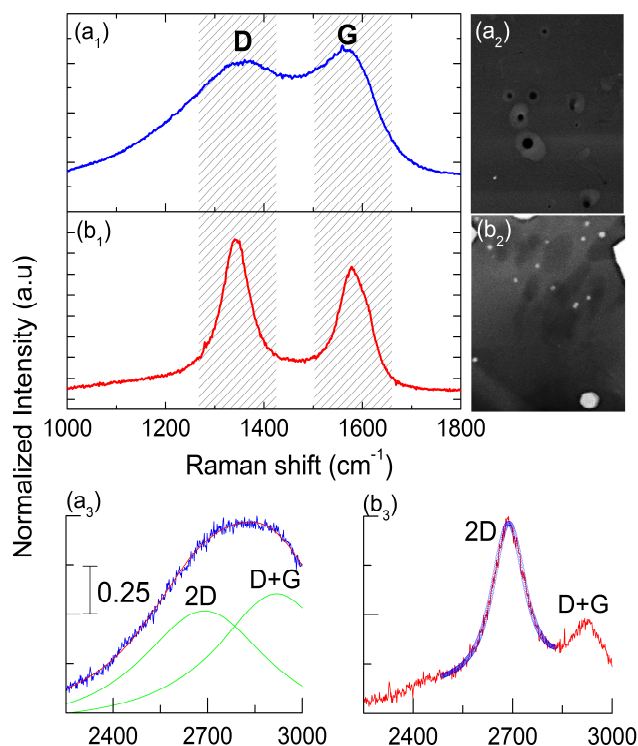


Fig. 5 Raman scattering D and G-band spectra of (a₁) the surface of carbon support (a₂) after pyrolysis and (b₁) of pinhole formation within carbonized support (b₂) together with their associated shift and deconvolution in 2D and D+G phonons with increased graphitization and layer coupling, in (a₃) and (b₃).

3.4 Surface enhanced Raman scattering from supported Re NPs

The resulting high-index NPs in graphitic carbon was also examined for surface enhanced Raman scattering as a NP-loaded composite. Raman scattering measurements of the support high index NPs were also acquired where the spectral response was taken from regions shown in Fig. 6 which is a HREM image of the overall region where the NP clusters of the region analysed. The background emission from dye coated carbon was accounted for in assessing the effective enhancement due to the presence of Re NPs.

The spectra, shown in Fig. 6, confirm significant enhancement

of the scattering cross-section where specific Raman shifts of MV10B undergo intensity increases and improved resolution⁵⁰⁻⁵²; the clear detection of in plane aromatic C–H bending, the phenyl C–N stretching and in-plane C–H bending and also out of phase in-plane carbon ring stretches at 1575 and 1617 cm⁻¹. While some of the scattering processes are in near resonance Raman conditions, the SERS effect is predominantly found for Re NP loaded regions of the otherwise entirely dye functionalized porous support. The substrate enhancement factor EF (as opposed to absolute enhancement factors) can thus be estimated following the more rigorous approach summarised by Le Ru *et al.*⁵³ given by

$$EF = \left[\frac{I_{SERS}}{I_{RS}} \right] \cdot \left(\frac{c_{RS} H_{eff}}{\mu_m \mu_s A_M} \right)$$

where I_{SERS} and I_{RS} are the signal intensity under SERS and Raman conditions, respectively, c_{RS} is the concentration of the solution and H_{eff} is the effective height of the scattering volume, μ_M is the surface density of the nanostructures with μ_s being the surface density of molecules, and A_M is the surface area in each metallic structure. With this, EF is in the range $3 - 7 \times 10^2$. Such enhancement has not been observed for Re, which weakly holds plasmon polaritons, and carbon functionalised Re (as opposed to Re within a carbon host) has been shown to have severe extinction of its absorption peak. Absolute enhancement factors are more difficult to assess due to the complicated composite nature of the material, but typically are many order of magnitude greater than corresponding substrate enhancement factors⁵⁴. As the dye functionalized the entire porous carbon support, the enhancement factor was also estimated from the Raman signal rate considering the ratio of the measured intensity and that of a single dye molecule (which contributes just $I_{RS} = 6.3 \times 10^{-7} \text{ s}^{-1}$ to the signal rate^{55,56} corresponding to Raman cross-section of $\sim 3.6 \times 10^{-26} \text{ cm}^2 \text{ sr}^{-1}$) for a predefined signal collection time according to⁵⁷

$$EF = \frac{I_{SERS}}{I_{RS}} \cdot \frac{1}{N_{MV} t}$$

Here, the background Raman signal rate for porous carbon only has been accounted for. Using the MV molecular footprint area of 3.51 nm² per molecule⁵⁵ $\sim 3.12 \times 10^5$ molecules are probed in the areal beam waist of 1.22λ/N.A. $\sim 1.1 \mu\text{m}^2$. The EF estimated by considering the density of dye molecules rather than the substrate is thus estimated to be $\sim 3-4 \times 10^3$. We stress that the complicated 3D nature of the material means that this estimated is likely the largest enhancement to be found and the difference in EF using both approaches is linked to the difficulty in accurately determining the effective density and adsorption area of the Re NPs. The EF however, is found to be sensitive to the NP size in agreement with electrochemically modified reduced graphene functionalized with Au NPs^{24, 58}; this EF is the highest measured and occurs for thin region of the carbon support and a high density of mixed NP sizes including NPs and the layered, high surface area supracrystals. For regions containing uniformly dispersed high-index NPs only, such as shown in Fig. 2b, negligible EM enhancement effects were found.

The time evolution of the intensity of the peak at ~1575 cm⁻¹, shown in Fig. 6, confirms that after irradiation for > 45 mins, the

SERS intensity begins to diminish.

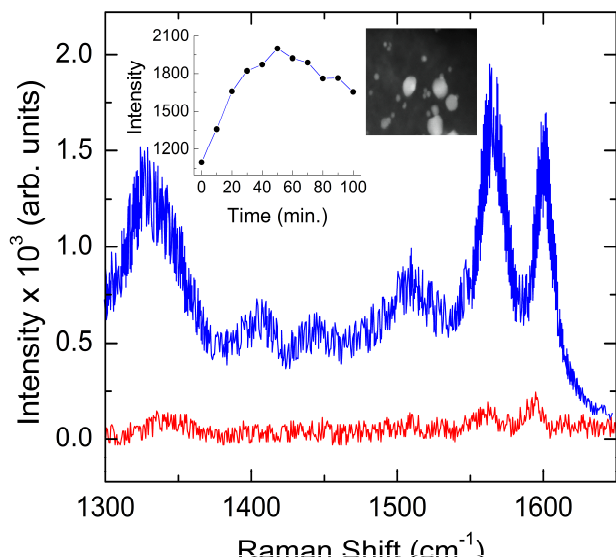


Fig. 6 SERS spectra of Methyl Violet 10B from supported high index Re NPs at the polymer-air interface at regions of high NP density (blue) and of low NP density (black). (Inset) Variation of the intensity of the peak at 1575 cm^{-1} with time; Dark field STEM image of NPs within the near surface region of the drop-cast deposit.

While difficult to monitor the position of NPs during SERS measurements, it is suggested that Joule heating from the beam (laser power density of $\sim 10^5 \text{ W m}^{-2}$, which is the limit at which heating affects for carbon start to be noticed) could allow some NPs to coarsen as they have been shown to do during direct heating, effectively reducing the density of proximal particles over time required for EM field enhancement. This effect would likely dominate over chemical enhancement at high NP loading, or cause thermolysis of the chemical attachment sites; both mechanisms would decrease the SERS activity.

4. Conclusions

A solution and surfactant-free route has been developed to grown high-index Re NPs by coarsening from an entropic-driven phase separation or demixing of a $\text{K}[\text{ReO}_4]/[\text{NP}(\text{O}_2\text{C}_{12}\text{H}_8)_3]$ composite. By demixing and nucleation of the metastable composite polymer, high index Re NPs are seeded, incubated and ripened through crystallization within a cyclic matrix from pyrolyzed cyclic phosphazene that converts to a solid graphitic carbon NP support in a single step during pyrolysis. The method relieves the constraint on solution based methods that use surfactants to control particle size and shape and the approach can be directly applied to other metals capable of either coordination to an organometallic derivative of a polymeric, oligomeric or cyclic phosphazene, or as a metal-polymer mixture. This solid state method allows supracrystal formation from ripening of Re NPs, the density and structure of either of these being tunable by the polymer type and mixture composition. This marriage of polymer microphase demixing and nanocrystal growth in the complete absence of functional ligands or liquids may lead to a variety of high index NPs, nanocrystal dispersions and homogeneous supracrystals on surfaces or directly within its host support.

When the host is layered graphite, this method could

potentially be refined to give 3D metal or metal oxide functionalised graphitic frameworks similar to metal NP functionalised graphene, which very recently showed significant photovoltage enhancement by plasmonic interactions. As the method has useful parallels to dewetting mechanisms, it could also form a test-bed for complex shaped metallic nanoparticle and nanocrystal growth, and for investigations of metallic supracrystal growth in the complete absence of liquids for growth, or for liquid-mediated competitive free energy minimization of NP colloids using surfactants and van der Waals forces between NPs. The demixing, dewetting and solidification define the ripening of the NPs with the matrix defined by its decomposition chemistry. Finally, NP dispersions on the surface of surface deposited dispersion of Re NPs exhibit surface enhanced Raman scattering as a supported dispersion of NP, improving detection scattering cross-sections for probe molecules.

Notes and references

- ^a Departamento de Química, Facultad de Química, Universidad de Chile, La Palmeras 3425, Nuñoa, Casilla 653, Santiago de Chile, Chile. Fax: +56 2 2713888; Tel: +56 2 9787367; E-mail: cdiaz@uchile.cl.
 - ^b Universidad Andres Bello, Departamento de Ciencias Químicas, Facultad de Ciencias Exactas. Av. Republica 275, Santiago, Chile.
 - ^c Applied Nanoscience Group, Department of Chemistry, University College Cork, Cork, Ireland. Fax: +353 21 4274097; Tel: +353 21 490 2732; E-mail: c.odwyer@ucc.ie.
 - ^d Micro & Nanoelectronics Centre, Tyndall National Institute, Lee Maltings, Cork, Ireland.
- †Electronic Supplementary Information (ESI) available: HRTEM, SEM, STEM and EDX of Re nanoparticles. See DOI: 10.1039/b000000x/.
- ‡This work was supported by Fondecyt grants 1120179 and 1095135. Part of this work was conducted under the framework of the INSPIRE programme, funded by the Irish Government's Programme for Research in Third Level Institutions, Cycle 4, National Development Plan 2007-2013. This work was also supported by Science Foundation Ireland under contract no. 07/SK/B1232a. The authors thank Dr Calum Dickinson for assistance with HREM analysis.
- T. K. Sau and A. L. Rogach, *Complex shaped metal nanoparticles – Bottom-up syntheses and applications*, Wiley-VCH, Weinheim, Germany, 2012.
 - Y. G. Sun and Y. N. Xia, *Science*, 2002, **298**, 2176–2179.
 - M. A. Mahmoud and M. A. El-Sayed, *Nano Lett.*, 2011, **11**, 946.
 - K. Tedsree, C. W. A. Chan, S. Jones, Q. Cuan, W.-K. Li, X.-Q. Gong and S. C. E. Tsang, *Science*, 2011, **332**, 224.
 - E. Dreaden, X. Huang, A. M. Alkilany, C. J. Murphy and M. A. El-Sayed, *Chem. Soc. Rev.*, 2012, **41**, 2740–2779.
 - H. Liu, L. Zhang, X. Lang, Y. Yamaguchi, H. Iwasaki, Y. Inouye, Q. Xue and M. Chen, *Sci. Rep.*, 2011, **1**, 112.
 - J. Zhang, M. R. Langille and C. A. Mirkin, *Nano Lett.*, 2011, **11**, 2495.
 - T. K. Sau and C. J. Murphy, *J. Am. Chem. Soc.*, 2004, **126**, 8648–8649.
 - X. Wang, J. Zhuang, Q. Peng and Y. Li, *Nature*, 2005, **437**, 121–124.
 - M. R. Langille, J. Zhang, M. L. Personick, S. Li and C. A. Mirkin, *Science*, 2012, **337**, 954–957.
 - J. M. Yuk, J. Park, P. Ercius, K. Kim, D. J. Hellebusch, M. F. Crommie, J. Y. Lee, A. Zettl and A. P. Alivisatos, *Science*, 2012, **336**, 61–64.
 - S. C. Glotzer and M. J. Solomon, *Nat. Mater.*, 2007, **6**, 557–562.
 - Y. Yu, Q. Zhang, J. Xie, X. Lu and J. Y. Lee, *Nanoscale*, 2011, **3**, 1497–1500.
 - B. L. V. Prasad, C. M. Sorensen and K. J. Klabunde, *Chem. Soc. Rev.*, 2008, **37**, 1871.
 - M. P. Pileni, *J. Phys. Chem. B*, 2001, **105**, 3358.
 - M. P. Pileni, *Acc. Chem. Res.*, 2008, **41**, 1799.

17. A. R. Tao, D. P. Ceperley, P. Sinsermsuksakul, A. R. Neureuther and P. Yang, *Nano Lett.*, 2008, **8**, 4033.
18. Z. Nie, A. Petukhova and E. Kumacheva, *Nat. Nanotechnol.*, 2009, **5**, 15.
19. S. Nie and S. R. Emory, *Science*, 1997, **275**, 1102.
20. T. J. Echtermeyer, L. Britnell, P. K. Jasnós, A. Lombardo, R. V. Gorbachev, A. N. Grigorenko, A. K. Geim, A. C. Ferrari and K. S. Novoselov, *Nat. Commun.*, 2011, **2**, 458.
21. N. Zhang, Y. Zhang and Y.-J. Xu, *Nanoscale*, 2012.
22. G. Duan, W. Cai, Y. Luo, Y. Li and Y. Lei, *Appl. Phys. Lett.*, 2006, **89**, 181918.
23. Y. Li, N. Koshizaki, H. Wang and Y. Shimizu, *ACS Nano*, 2011, **5**, 9403.
24. Y. Hu, L. Lu, J. Liu and W. Chen, *J. Mater. Chem.*, 2012, **22**, 11994.
25. X. Ling, L. M. Xie, Y. Fang, H. Xu, H. L. Zhang, J. Kong, M. S. Dresselhaus, J. Zhang and Z. F. Liu, *Nano Lett.*, 2010, **10**, 553.
26. C. Vollmer, E. Redel, K. Abu-Shandi, R. Thomann, H. Manyar, C. Hardacre and C. Janiak, *Chem. Eur. J.*, 2010, **16**, 3849.
27. E. L. Kunkes, D. A. Simonetti, J. A. Dumesic, W. D. Pyrz, L. E. Murillo, J. G. Chen and D. J. Buttrey, *J. Catal.*, 2008, **260**, 164.
28. A. Naumov, *Russ. J. Non-Ferrous Metals*, 2007, **48**, 418.
29. Y. Y. Chong, W. Y. Chow and W. Y. Fan, *J. Colloid Interface Sci.*, 2012, **369**, 164-169.
30. R. R. Dykeman, N. Yan, R. Scopelliti and P. J. Dyson, *Inorg. Chem.*, 2011, **50**, 717.
31. G. A. Carriedo, L. Fernández-Catuxo, F. J. G. Alonso, P. Gómez-Elipe and P. A. González, *Macromolecules*, 1996, **29**, 5320-5325.
32. M. R. Langille, M. L. Personick, J. Zhang and C. A. Mirkin, *J. Am. Chem. Soc.*, 2011, **133**, 10414-10417.
33. Z.-Y. Zhou, N. Tian, J.-T. Li, I. Broadwell and S.-G. Sun, *Chem. Soc. Rev.*, 2011, **40**, 4167-4185.
34. R. Mukherjee, S. Das, A. Das, S. K. Sharma, A. K. Raychaudhuri and A. Sharma, *ACS Nano*, 2010, **4**, 3709-3724.
35. L. Meli and P. F. Green, *ACS Nano*, 2008, **2**, 1305-1312.
36. C. Díaz, M. L. Valenzuela, V. Lavayen and C. O'Dwyer, *Inorg. Chem.*, 2012, **51**, 6228-6236.
37. B. C. Tappan, M. H. Huynh, M. A. Hiskey, D. E. Chavez, E. P. Luther, J. T. Mang and S. F. Son, *J. Am. Chem. Soc.*, 2006, **128**, 6589.
38. C. Díaz, M. L. Valenzuela, A. Laguna, V. Lavayen, J. Jiménez, L. A. Power and C. O'Dwyer, *Langmuir*, 2010, **26**, 10223-10233.
39. C. Valenzuela, G. Carriedo, M. Luisa Valenzuela, L. Zúñiga and C. O'Dwyer, *J. Inorg. Org. Polym. Mater.*, 2012, **22**, 447-454.
40. C. Diaz, M. L. Valenzuela, D. Bravo, V. Lavayen and C. O'Dwyer, *Inorg. Chem.*, 2008, **47**, 11561.
41. N. Tian, Z.-Y. Zhou, S.-G. Sun, Y. Ding and Z. L. Wang, *Science*, 2007, **316**, 732-735.
42. D. Kim, Y. W. Lee, S. B. Lee and S. W. Han, *Angew. Chem. Int. Ed.*, 2012, **51**, 159-163.
43. C. J. DeSantis, A. C. Sue, M. M. Bower and S. E. Skrabalak, *ACS Nano*, 2012, **6**, 2617-2628.
44. C. Díaz, M. L. Valenzuela, D. Bravo, C. Dickinson and C. O'Dwyer, *J. Colloid Interface Sci.*, 2011, **362**, 21-32.
45. H. Alhumiany, S. Jarvis, R. A. J. Woolley, A. Stannard, M. Blunt and P. Moriarty, *J. Mater. Chem.*, 2011, **21**, 16983.
46. D. H. Cole, K. R. Shull, P. Baldo and L. Rehn, *Macromolecules*, 1999, **32**, 771-779.
47. H. C. Wong and J. T. Cabral, *Macromolecules*, 2011, **44**, 4530-4537.
48. B. A. Korgel, *Phys. Rev. Lett.*, 2001, **86**, 127.
49. M. S. Dresselhaus, A. Jorio, M. Hofmann, G. Dresselhaus and R. Saito, *Nano Lett.*, 2010, **10**, 751-758.
50. Y. C. Cao, R. Jin and C. A. Mirkin, *Science*, 2002, **297**, 1536.
51. L. M. Liz-Marzán, *Langmuir*, 2006, **22**, 32-41.
52. J. A. Dieringer, K. L. Wustholz, D. J. Masiello, J. P. Camden, S. L. Kleinman, G. C. Schatz and R. P. Van Duyne, *J. Am. Chem. Soc.*, 2009, **131**, 849.
53. E. C. L. Ru, E. Blackie, M. Meyer and P. G. Etchegoin, *J. Phys. Chem. C*, 2007, **111**, 13794.
54. K. Kneipp, H. Kneipp, I. Itzkan, R. Dasari and M. Feld, *J. Phys.: Condens. Matter*, 2002, **14**, R597.
55. K. Hofflich, M. Becker, G. Leuchs and S. Christiansen, *Nanotechnology*, 2012, **23**, 185303.
56. K. Kneipp, *J. Phys. Chem. C*, 2002, **111**, 13794.
57. J. A. Schuller, E. S. Barnard, W. Cui, Y. C. Jun, J. S. White and M. L. Brongersma, *Nat. Mater.*, 2010, **9**, 193.
58. X. X. Yu, H. B. Cai, W. H. Zhang, X. J. Li, N. Pan, Y. Luo, X. P. Wang and J. G. Hou, *ACS Nano*, 2011, **5**, 952.